Published by IOP Publishing for Sissa Medialab

Received: *May 14, 2024*
Revised: *September 30, 2024*
Accepted: *December 24, 2024*
Published: *January 30, 2025*

The effect of radiation damage on the light yield and uniformity of candidate plastic scintillator tiles for the CMS hadron calorimeter upgrade

The CMS HCAL collaboration

E-mail: abelloni@umd.edu

Abstract: A study has been performed to understand the effects of radiation damage on various plastic scintillator tiles considered for a possible upgrade of the hadron calorimeter of the CMS detector. Measurements were made with unirradiated tiles and with tiles that had been irradiated in the CMS collision hall to a dose of 44 kGy. Results are presented for the tiles of different shapes in terms of the energy spectrum, efficiency as a function of the position at which each tile was hit, as well as light yield. All the tiles showed a light reduction of up to about 50%. The tiles with the shape currently used in the CMS detector did not see increased non-uniformity of light collection, while a significant disuniformity was observed for the tiles considered as alternatives.

Keywords: Calorimeters; Interaction of radiation with matter; Scintillators, scintillation and light emission processes (solid, gas and liquid scintillators); Calorimeter methods

ArXiv ePrint: 2207.11960

https://doi.org/10.1088/1748-0221/20/01/P01026

2025 JINST 20 P01026

Contents

1 Introduction

Modern large-scale particle physics experiments at high center-of-mass energies, such as ATLAS [1] and CMS [2] at the Large Hadron Collider (LHC) facility at CERN, use plastic scintillators for particle detection due to their low cost and large light yield. However, scintillators are subject to radiation damage, reducing their light yield [3, 4] over the time scale of the experiment. For example, the scintillating tiles in the endcap hadronic calorimeter (HE) of the CMS detector had a reduction of light output up to about 25% after the 2017 LHC operation, which corresponded to an integrated luminosity of 50 fb^{-1} [5] of proton-proton collisions, and a dose of approximately 1.5 kGy. It is anticipated that the scintillators in the hadron calorimeters for the proposed experiments at the future accelerators, such as FCC-hh, could receive doses up to 8 kGy or even 1 MGy [6]. Studies of the radiation effects on the transmission of light in plastic scintillators have been presented, for example, in ref. [7]. This study presents a continuation of the attempt to find a solution to the decreased light yield of the plastic scintillators in the CMS hadronic endcap calorimeter, which covers the rapidity region of $1.4 < |\eta| < 3$, where $\eta = -\ln\left(\tan\frac{\theta}{2}\right)$ and θ is the polar angle, measured with respect to the beam line.

Our previous paper [8] compared the performance of the tiles made from scintillator materials manufactured by the Eljen corporation[1] (EJ-200, EJ-260, with different dopant concentrations) to those used in the legacy calorimeter (SCSN-81 by Kuraray[2]) of the CMS detector; the production of Kuraray has since been discontinued. It is believed that the effects of radiation damage can be partially mitigated by either overdoping the material or by shifting the output to a longer wavelength region. The previous study confirmed that both of these were viable options for the replacement of the SCSN-81 tiles. We now present an assessment of how these materials perform when damaged by radiation. The irradiation was performed at the Castor Radiation Facility at CERN with the scintillator samples installed in the proximity of the LHC beam line. In addition to the two previous methods of mitigating the effects of radiation damage, a third possibility, using tiles of different shapes, is also checked. The light yield of the scintillator detectors is measured in terms of their response to minimum ionizing particles.

[1]Eljen Technology, 1300 W. Broadway, Sweetwater, TX 79556, United States.
[2]Kuraray, Ote Center Building,1-1-3, Otemachi, Chiyoda-ku, Tokyo, 100-8115, Japan.

2025 JINST 20 P01026

2 Experimental setup

The experimental setup is almost identical to the one in our previous study [8]. The data were collected in the North Area of the H2 Beam Line at the CERN Prevessin site using beam dumps from the Super Proton Synchrotron (SPS). A muon beam is generated from the decay of a 150 GeV charged pion beam. The beam path passes through several instruments for triggering and precise tracking on its way to the scintillator samples under test. In order of increasing distance from the beam extraction point, these are wire chamber "A", four large scintillating plastic trigger counters, and wire chamber "C". The wire chambers were the drift chambers described in ref. [8], with size ($100 \times 100\,\mathrm{mm}^2$) and resolutions of ≈ 0.5 mm in the transverse plane. Figure 1 shows the relative positions of the instruments, tiles, and beam. Only two of the wire chambers were active for this study, as opposed to the three used in ref. [8]. The yellow region indicates an instrumented 40° wedge of HCAL, which is not used in the analysis presented in this paper.

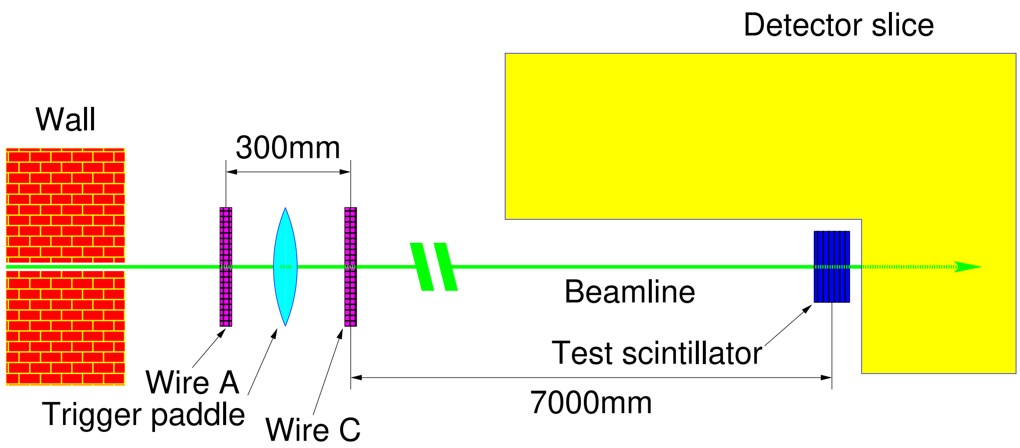

Figure 1. Diagram of the experimental area, not to scale.

The two wire chambers were aligned before use in the analysis. The hits in the wire chambers determine the points where the muons from the incident beam intersect the tiles. We assume that the muons in the experimental area travel along a straight line, and therefore the difference between the x and y measurements made in the two wire chambers is a Gaussian with mean zero. The distributions of the x and y measurements after the alignment are shown in figure 2.

The data acquisition system has front-end and back-end electronics designed for the Phase-I upgrade of the CMS hadron calorimeter (HCAL) with silicon photomultipliers (SiPMs) as the photodetectors. The system is described in detail in ref. [9]. The experimental setup is based on the Phase-I configuration of SiPM-equipped HCAL detectors, as reported in ref. [9, figure 1.7]. Each scintillator tile is connected to an individual SiPM (although in the CMS detector each SiPM receives scintillation light from multiple tiles). The light produced in the scintillator is transmitted via wavelength-shifting (WLS) fibers to silicon photomultiplier (SiPM) photodetectors. The SiPMs are custom-made by Hamamatsu Photonics[3] to fulfill the requirements for their usage in the HCAL subsystem of the CMS experiment. A detailed description of their characteristics is presented in

[3]Hamamatsu Photonics, 325-6, Sunayama-cho, Naka-ku, Hamamatsu City, Shizuoka, 430-8587, Japan.

2025 JINST 20 P01026

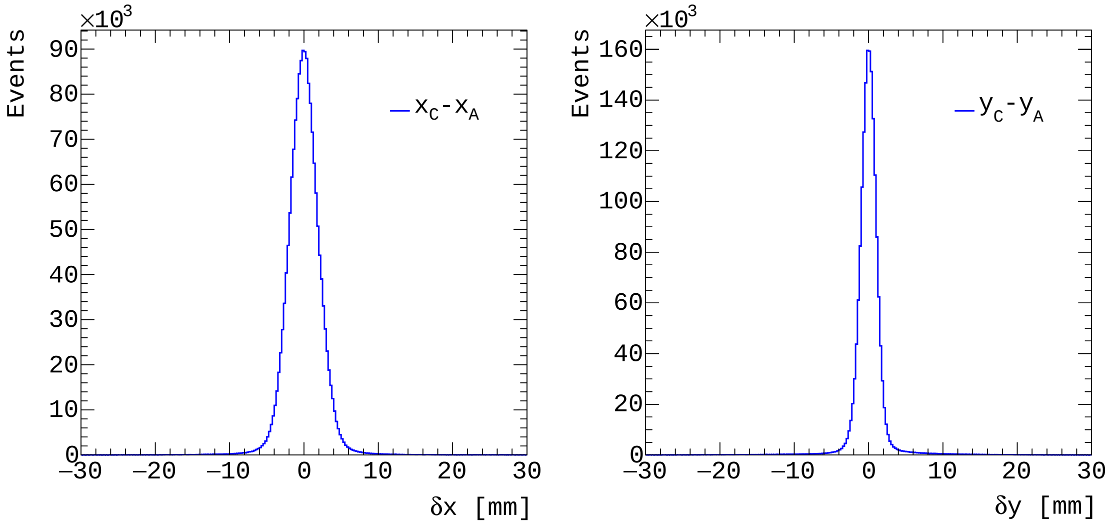

Figure 2. Difference in position of hits along the x (left) and y (right) directions for the two wire chambers. The distributions contain an offset correction calculated assuming that the muons travel along straight trajectories.

ref. [10]. The pulse of current generated by the SiPM is integrated using Charge-Integrator-and-Encoder (QIE10) chips [11–14], with the digitized signals collected by a Microsemi IGLOO2 FPGA and transmitted to the back-end electronics via an optical link through a versatile-link transmitter (VTTx) [15]. The VTTx connects each front-end (FE) module to an HCAL μTCA Trigger and Readout (μHTR) module. The encoded signals from the QIE10 chips and the wire chambers are reconstructed into events and saved to disk. Figure 3 indicates the path of the signal from the scintillator tiles to the storage via the digitization (QIE10), the alignment and formatting (Microsemi IGLOO2 FPGA), the data transmission (VTTx), the back-end electronics (uHTR).

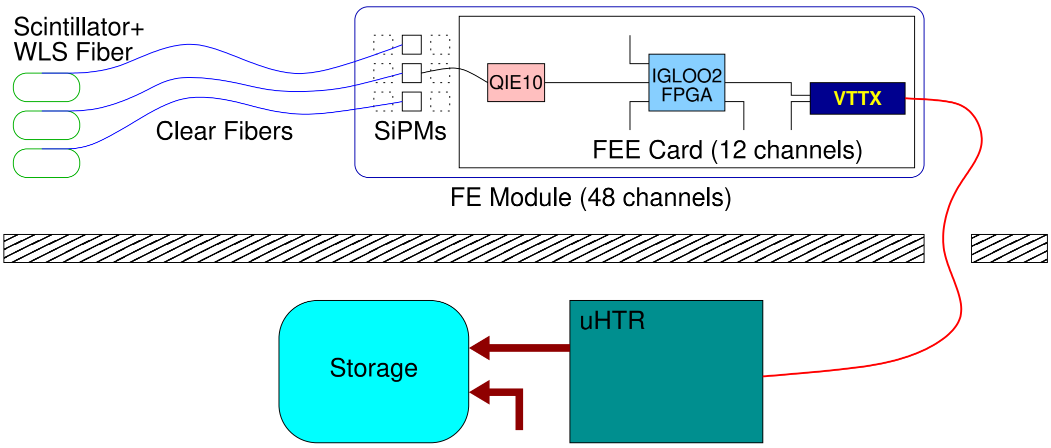

Figure 3. Overview of the data path at the H2 test beam facility at CERN.

The scintillator tiles had two types of grooves where WLS fibers are inserted to collect a fraction of the light produced in the tile. We refer to them as σ and *finger* tiles, respectively. A schematic drawing of the two formats is sketched in figure 4. The same figure provides a sectional view of the tile showing the groove within which the WLS fiber is installed. In the first case the WLS fiber

2025 JINST 20 P01026

roughly follows a σ-shaped path along the border of the σ tile, while for the second it goes straight through the middle of the finger tile. The σ tiles have areas of $10 \times 10\,\text{cm}^2$, while the finger tiles are $10 \times 2\,\text{cm}^2$. The thickness of the tiles were the same, about 0.4 cm.

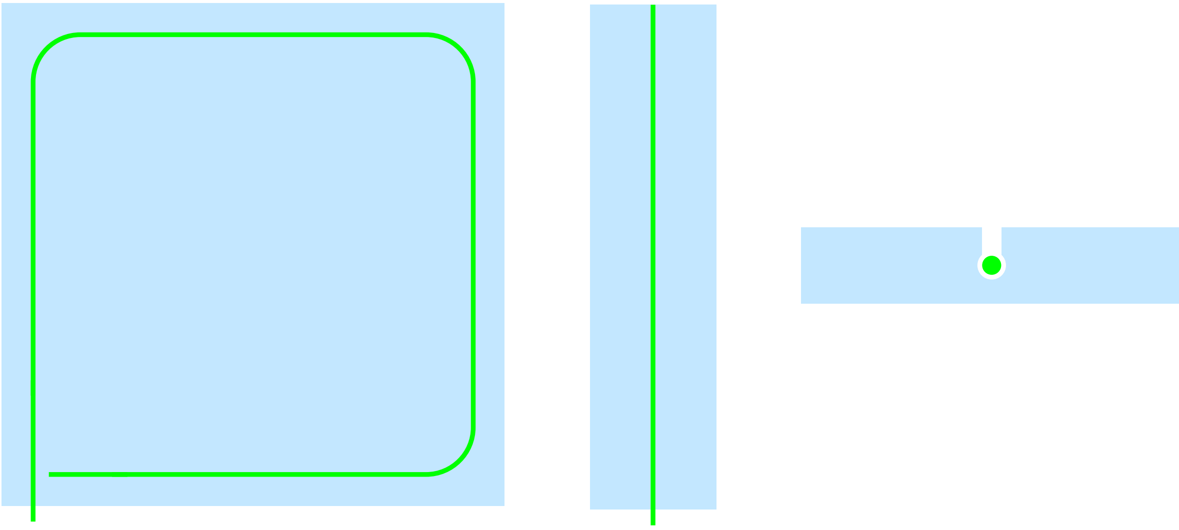

Figure 4. Schematic drawing of the σ (left) and finger (center) tiles and a sectional view of the groove within which the WLS fiber is installed.

A summary of the characteristics of the scintillator tiles used in this experiment is given in table 1. The Eljen scintillator tiles were exclusively available in σ-tile format, while SCSN-81 tiles were available in both σ- and finger-tile formats. The WLS fiber is Y11 for blue scintillators and O2 for green scintillators, both produced by Kuraray.

Table 1. Basic characteristics of the scintillator tiles used in this study. The tile color refers to the wavelength of maximum emission, i.e., 425 nm for the blue scintillators and 490 nm for the green. The irradiation was performed at the Castor Radiation Facility at CERN with the scintillator samples installed in the proximity of the LHC beam line. The base material of the Eljen (EJ) tiles is polyvinyl toluene (PVT), while polystyrene (PS) is used for the SCSN tiles, produced by Kuraray. The EJ tile marked by "†" contains a proprietary primary dopant, in a concentration about twice than available in commercial samples.

Tile	Base	Color	Format [cm^3]	Integrated dose [kGy]
EJ 200	PVT	Blue	$10 \times 10 \times 0.4$	not irradiated
EJ 260	PVT	Green	$10 \times 10 \times 0.4$	not irradiated
EJ 260 2P†	PVT	Green	$10 \times 10 \times 0.4$	not irradiated
SCSN 81F1	PS	Blue	$2 \times 10 \times 0.37$	44 ± 7
SCSN 81F2	PS	Blue	$2 \times 10 \times 0.37$	44 ± 7
SCSN 81F3	PS	Blue	$2 \times 10 \times 0.37$	44 ± 7
SCSN 81F4	PS	Blue	$2 \times 10 \times 0.37$	44 ± 7
SCSN 81S	PS	Blue	$10 \times 10 \times 0.37$	55 ± 9

The SCSN-81 tiles were subjected to irradiation before being included in the test-beam measurement. They were placed in the CMS collision hall on the structure that housed the CMS forward

2025 JINST 20 P01026

calorimeter CASTOR [16], 14.3 m away from the CMS interaction point, and at a distance between 13.1 and 14.4 cm from the LHC beam line. The total integrated dose was measured using FWT-60-00 Radiachromic dosimeters (thin films) by Far West Technology, which were attached to the top of the scintillator samples. The uncertainty in the radiation dose is estimated to be 15%.

3 Data analysis

Prior to any selection, the data consisted of about 7 million triggered events. Events are required to have a single muon hitting both wire chambers. This ensures that the energy corresponds to a single minimum-ionizing particle (MIP) signal and allows the measurement of the detection efficiency as a function of the hit position on a tile. This requirement reduces the event sample to 1,720,742 events for the subsequent analysis. The finger tiles were not used until a later stage of the data taking operation; hence the corresponding sample contained only about 2.8 million events, which reduced to just 622,635 events after applying the requirement of single-muon traversal.

The data acquisition system measures a charge, corresponding to the time-integrated current from the SiPM photosensors in 25 ns time slices. The integrated charge is proportional to the number of photoelectrons, which in turn is proportional to the energy deposited by a MIP that crosses the scintillator. Figure 5 shows the measured pedestal-subtracted average charge in each of ten time slices for the finger tiles and for the σ tiles. Time slices 5 through 9 are used in the subsequent analysis to maximize the signal to noise ratio. From these plots it can be seen that all tiles were timed-in similarly and the same time slices are therefore used for each tile.

The event-by-event per-time-slice pedestal is estimated by averaging the charge integrated in the first three time slices. Unless otherwise noted, the event-by-event pedestal is estimated by multiplying the per-time-slice pedestal value estimated above by the number of time slices that are added to obtain the total integrated charge in the event, i.e., time slices 5 through 9.

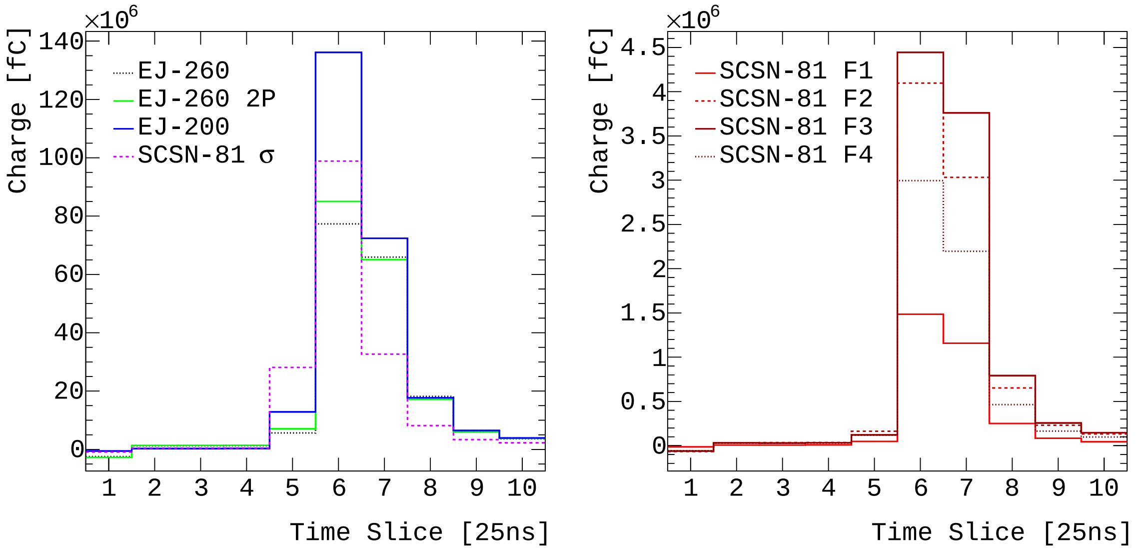

Figure 5. Average integrated SiPM charge in 25 ns time slices for σ tiles (left) and finger tiles (right) in a muon beam.

3.1 Hit efficiency

Each hit is represented by a two-dimensional (2D) point denoted by x and y coordinates in a plane perpendicular to the beam. The hit efficiency is defined to be the ratio of the number of events recorded with an integrated pulse greater than 25 fC, which is the value that separates the pedestal peak from the signal peak corresponding to one photoelectron, to the total number of recorded events that satisfy the single-muon traversal requirement. Two-dimensional efficiency maps are generated for each scintillator. The efficiency maps are also used to define a fiducial region, identifying the position of each tile relative to the beam spot. The lines marking the fiducial region are drawn through the region where the efficiency appeared to be at least $\approx 50\%$, and correspond to the estimated position of the physical boundary of the tiles. Figure 6 shows the efficiency maps for the EJ-260 and the second SCSN-81 finger tile, where the fiducial regions are identified by the dashed lines.

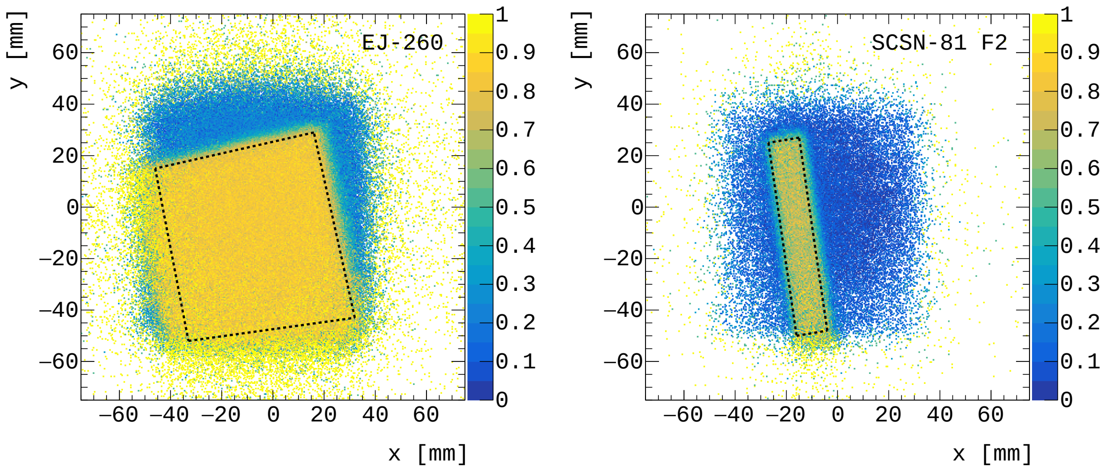

Figure 6. Maps of 2D efficiency for EJ-260 (left) and the second SCSN-81 finger tile (right). The dashed lines indicate the fiducial region that corresponds approximately to the overlap between the tile area and the beam, positioned along a path in which the hit efficiency, determined from the ratio of hits with an integrated pulse > 25 fC, divided by all the hits in the same bin, is $> 50\%$. Similar maps have been produced for the other scintillator samples.

The distributions in the pedestal levels, normalized to a single time slice, are shown in figure 7. They appear to follow two distinct trends, which are likely due to a different amount of light leaking through the connections, as the two sets of SiPMs are attached to different SiPM arrays by two separate fiber bundles. The equally spaced peaks correspond to an increasing number of photoelectrons. It is appropriate to note that the spacing between peaks is consistent among all SiPMs, which indicates that they have similar particle-detection efficiencies.

3.2 Energy spectra and efficiency maps

The fiducial regions defined in the previous sections are used to obtain a more accurate picture of the amount of energy collected by the tile from each muon that interacted with the plastic scintillator. Unless stated to the contrary, it is assumed that each event is selected by requiring the presence of a single muon within the fiducial region of each tile. Figures 8 and 9 show the integrated charge spectra for fiducial muons in all of the tiles used in our study. The efficiency ϵ, introduced in section 3.1,

2025 JINST 20 P01026

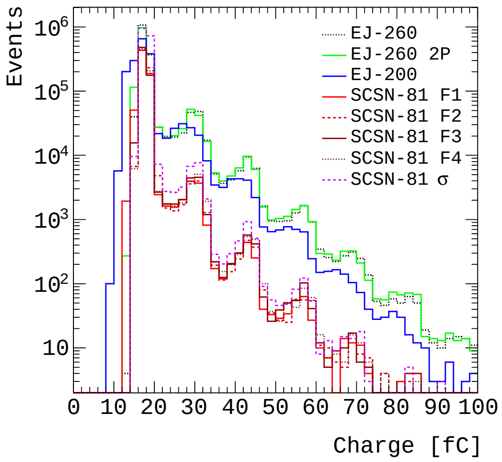

Figure 7. Event-by-event measurement of pedestal integrated charge, normalized to a single time slice. The distributions follow two distinct trends, which correspond to different SiPM arrays to which the scintillator tiles are connected.

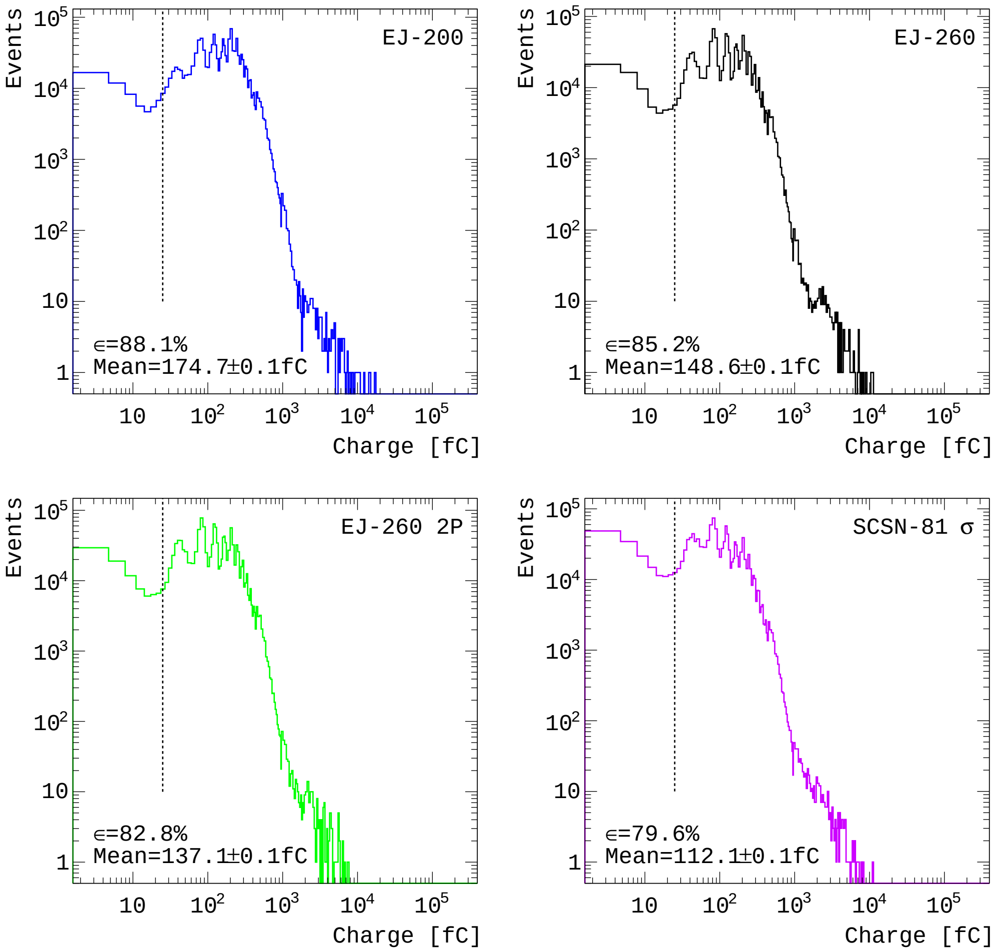

Figure 8. Integrated charge spectra for the σ tiles studied. The dashed lines indicate the threshold, set at 25 fC, above which a hit is considered to correspond to a MIP (muon).

2025 JINST 20 P01026

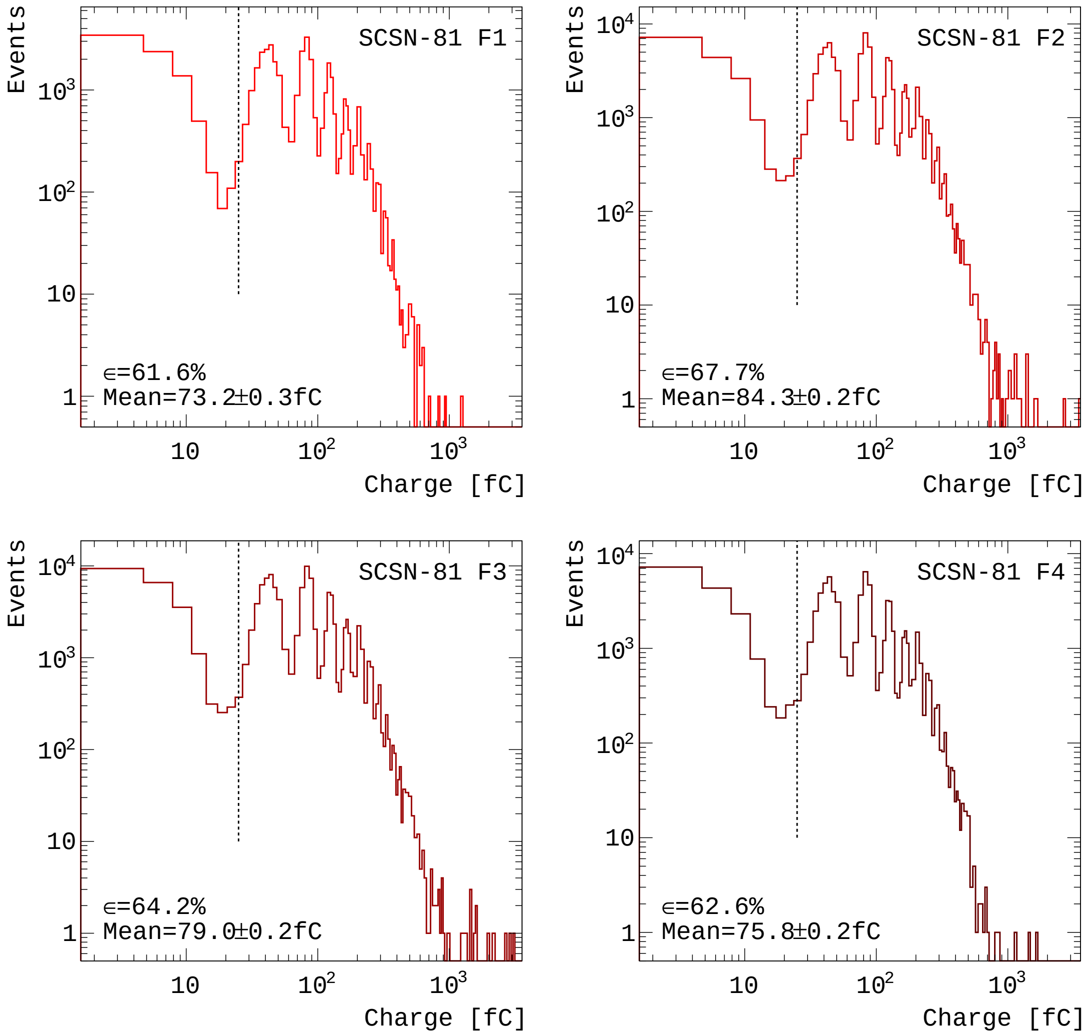

Figure 9. Integrated charge spectra for the finger tiles studied. The dashed lines indicate the threshold, set at 25 fC, above which a hit is considered to correspond to a MIP (muon).

is defined to be the ratio of the number of hits with an integrated pulse above the noise threshold, set at 25 fC, divided by the total number of hits.

For each type of tile, the 2D efficiency plots are shown in figures 10 and 11. The x and y axes have been rotated so that the finger tiles point vertically, and the sides of the σ tiles are parallel to the new axes. The efficiency plots do not show any significant dependence on x or y. The efficiency is defined in each bin to be the ratio of the number of hits with an integrated pulse above 25 fC, divided by the total number of hits. The dashed lines enclose the fiducial region, for which the efficiency is at least 50%.

To enhance any effects of non-uniformity in efficiency, possibly caused by radiation damage in the irradiated tiles, projections of the 2D efficiency maps along the x and y axes are shown in figure 12. In fact, a small decrease in efficiency in the middle section of the σ tiles can be seen in the region farthest from the wavelength-shifting fibers used to collect the scintillation light. The finger tiles display a clear reduction in the light yield the farther away the hits are from the top of the scintillator tile. This suggests that the wavelength-shifting fiber may be damaged, as the light produced in the lower section

2025 JINST 20 P01026

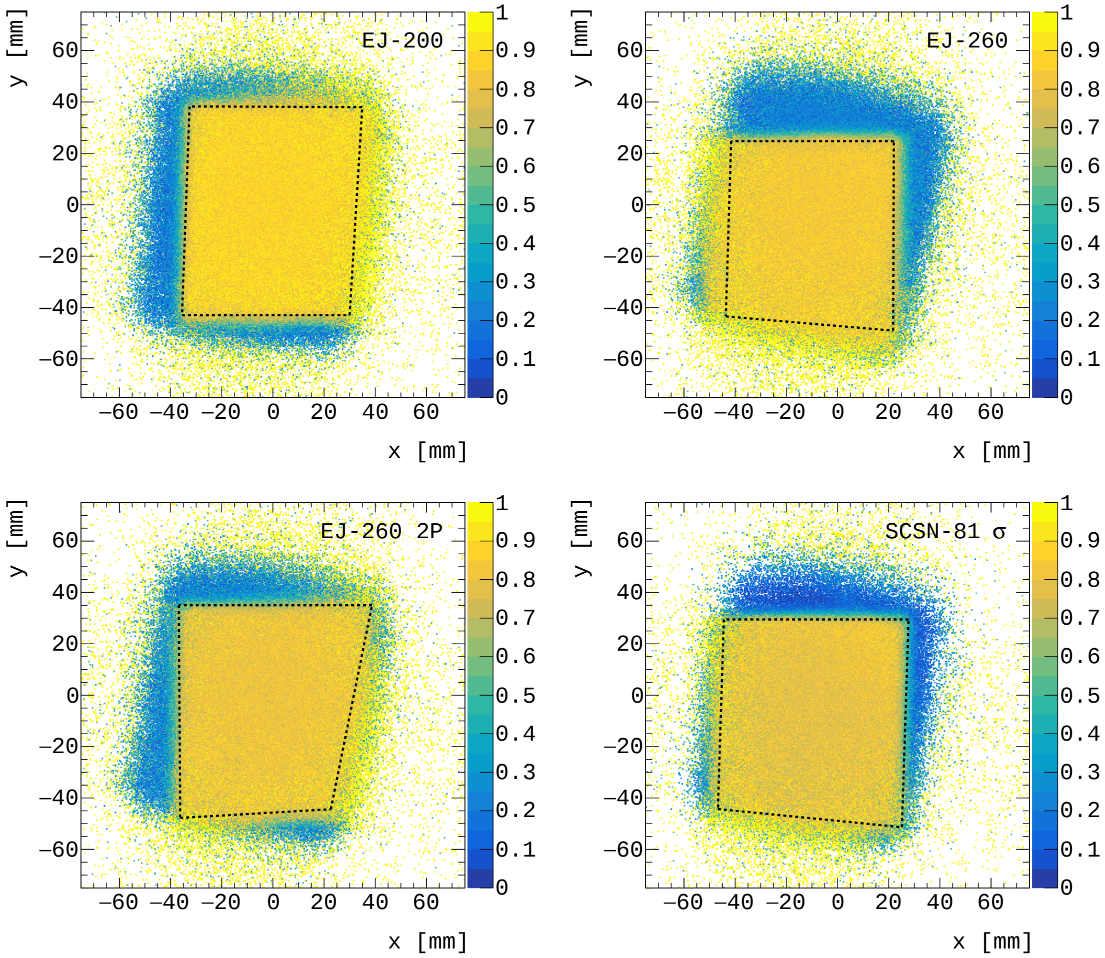

Figure 10. Efficiency maps for the σ tiles studied. The dashed lines indicate the fiducial region that corresponds approximately to the overlap between the tile area and the beam, positioned along a path in which the hit efficiency, determined from the ratio of hits with an integrated pulse > 25 fC, divided by all the hits in the same bin, is $> 50\%$.

of the finger tile has to travel a longer distance along that fiber. Measurements at the University of Maryland using a collimated Sr-90 source confirmed the trends observed in the test-beam data.

3.3 Light yield

The light yield in each tile is a parameter of interest, which, in addition to the hit efficiency, characterizes the performance of a scintillator. The light yield is defined as the average number of photons collected in the tile from each incident muon. Each muon releases approximately the same amount of energy in each tile. As indicated in table 1, the Eljen tiles are 4 mm thick, while the SCSN tiles are 3.7 mm thick. Hence, it is expected that a MIP deposits $\approx 9\%$ more energy while traversing an Eljen tile than a SCSN one; this aspect should be taken into consideration when comparing the light yields among the different scintillator tiles.

The charge distributions present a set of peaks at a fixed distance relative to each other, as is clearly seen, for example, in figure 13. Each subsequent peak corresponds to a higher number of photons. We discuss below two methods used to obtain a robust estimation of the light yield.

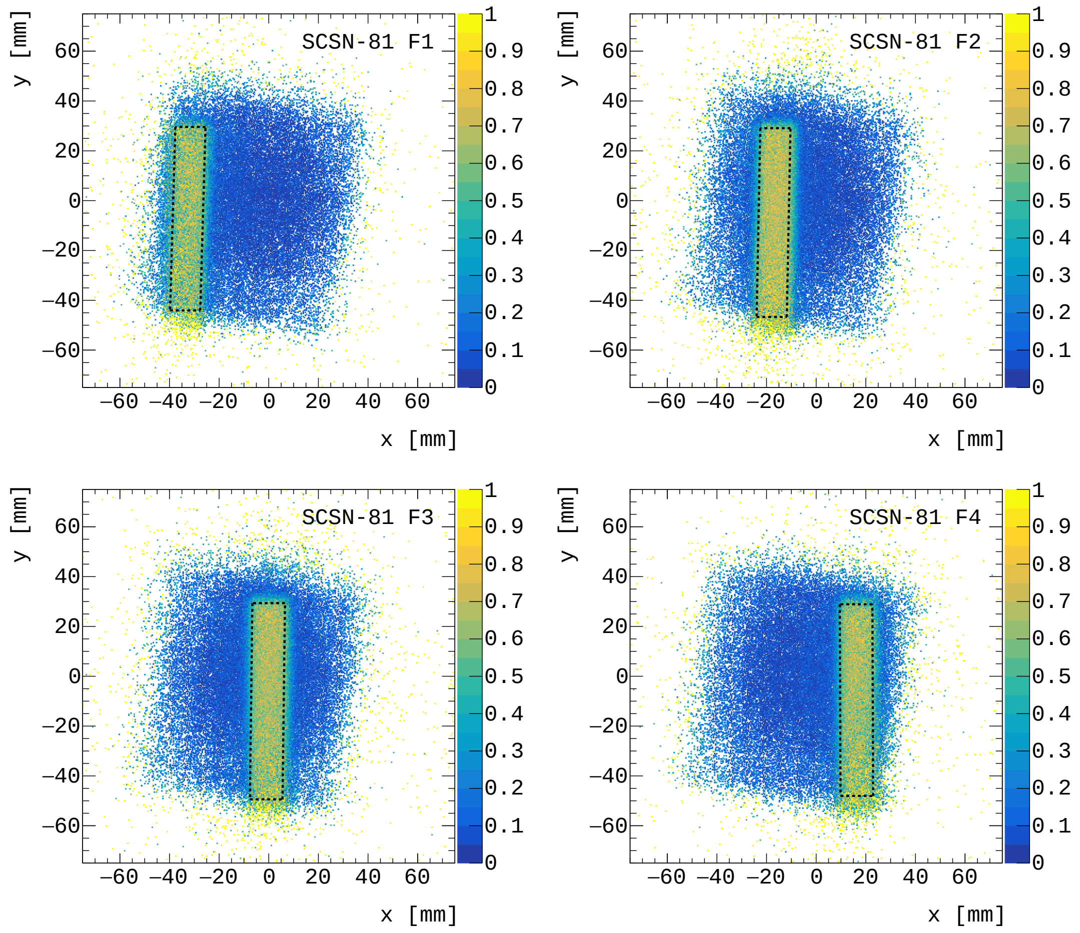

Figure 11. Efficiency maps for the finger tiles studied. The dashed lines indicate the fiducial region that corresponds approximately to the overlap between the tile area and the beam, positioned along a path in which the hit efficiency, determined from the ratio of hits with an integrated pulse > 25 fC, divided by all the hits in the same bin, is $> 50\%$.

Method I — Integration of contributions. The charge distribution shows a series of equally spaced Gaussian contributions of similar widths. Assuming that these contributions have the same separation, we can estimate the average number of photoelectrons by dividing the integrated signals of the charge spectrum by the distance between neighboring peaks, starting at 25 fC to eliminate the pedestal peak, and defining thereby the mean signal produced by just one photoelectron as the corresponding distance between neighboring peaks. We estimate this to be ≈ 41 fC.

A simple fit of the charge distribution using a sum of Gaussian functions, covering the whole spectrum, provides a cross check of the result obtained. Two examples of the fitted spectra are presented in figure 13. The two representative fits capture the main features of SiPM spectra: the distance between neighboring Gaussian peaks is consistent with a constant value; the width of the Gaussian peaks monotonically increases as they correspond to a higher number of photoelectrons. The latter is not the case for the last three Gaussians in the SCSN-81 finger-tile sample. Those Gaussians count for less than 1% of the number of events, indicating that the simplified fit model is suitable to extract approximate estimates of the scintillator performance.

2025 JINST 20 P01026

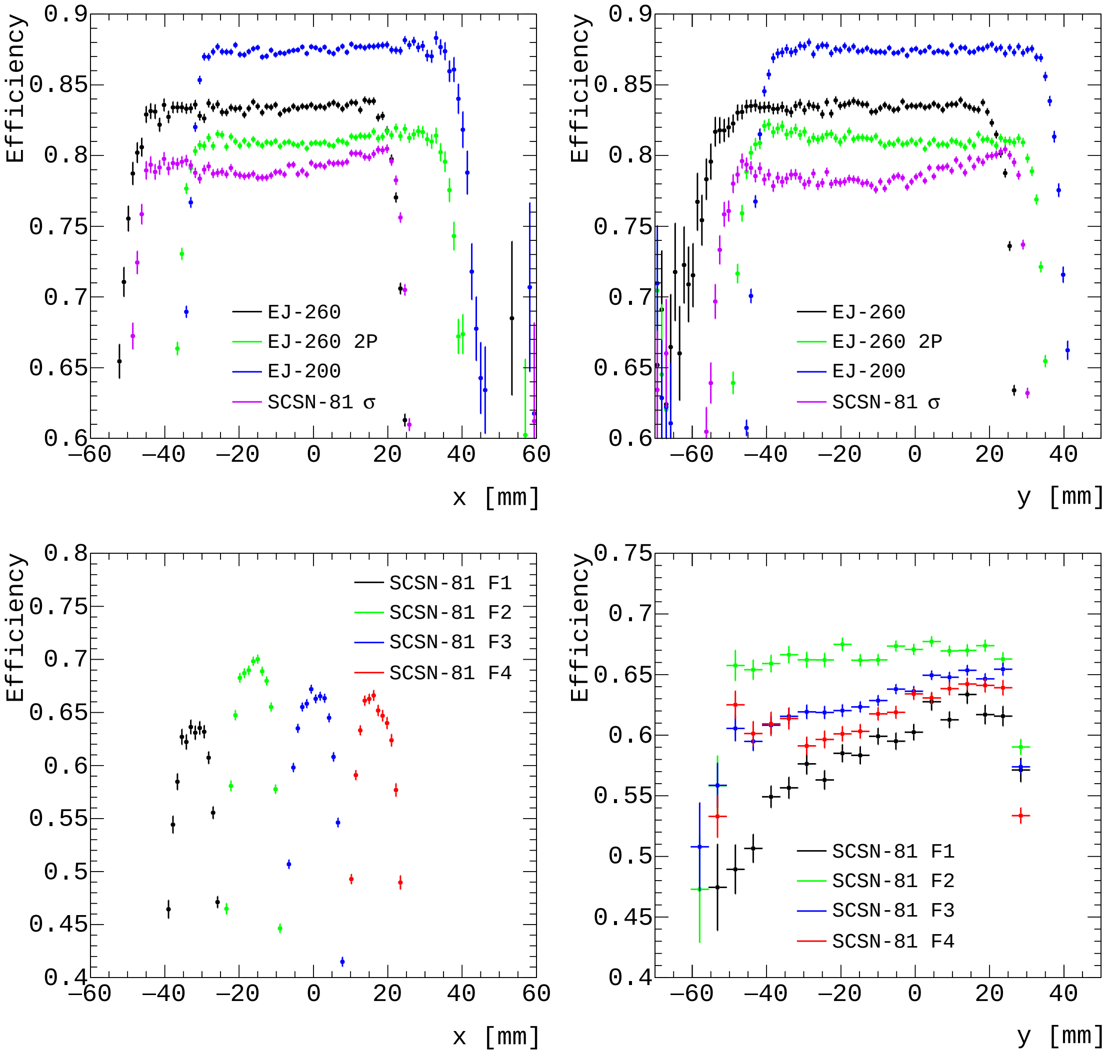

Figure 12. x (left) and y (right) efficiencies for σ tiles (top) and finger tiles (bottom).

It is to be noted, however, that the multi-Gaussian fit underestimates the yields relative to the integral-of-contributions method by $\approx 1-5\%$, partially because of the tail at high charge, where it is not possible to fit additional Gaussian functions properly. The comparison indicates that the integral-of-contribution method is robust.

Method II — Functional-form fit. The second method is based on a fit to the charge spectra using a function presented in ref. [17]. The RooFit framework [18] defines the probability density function that is used to perform an unbinned maximum likelihood fit. The fit parameters include the average number of initially emitted photo-electrons, the distance between neighboring peaks, and the cross-talk probability. It is important to note that the average number of photoelectrons returned by the fit is not compared directly with the number obtained with the other method described above; the latter include all the secondary emissions. As a first-order approximation, the results of the first method are compared to the number of initially emitted photoelectrons divided by $1-\chi$, where χ is the cross-talk probability. The fit also estimates the distance between neighboring peaks. In all cases,

2025 JINST 20 P01026

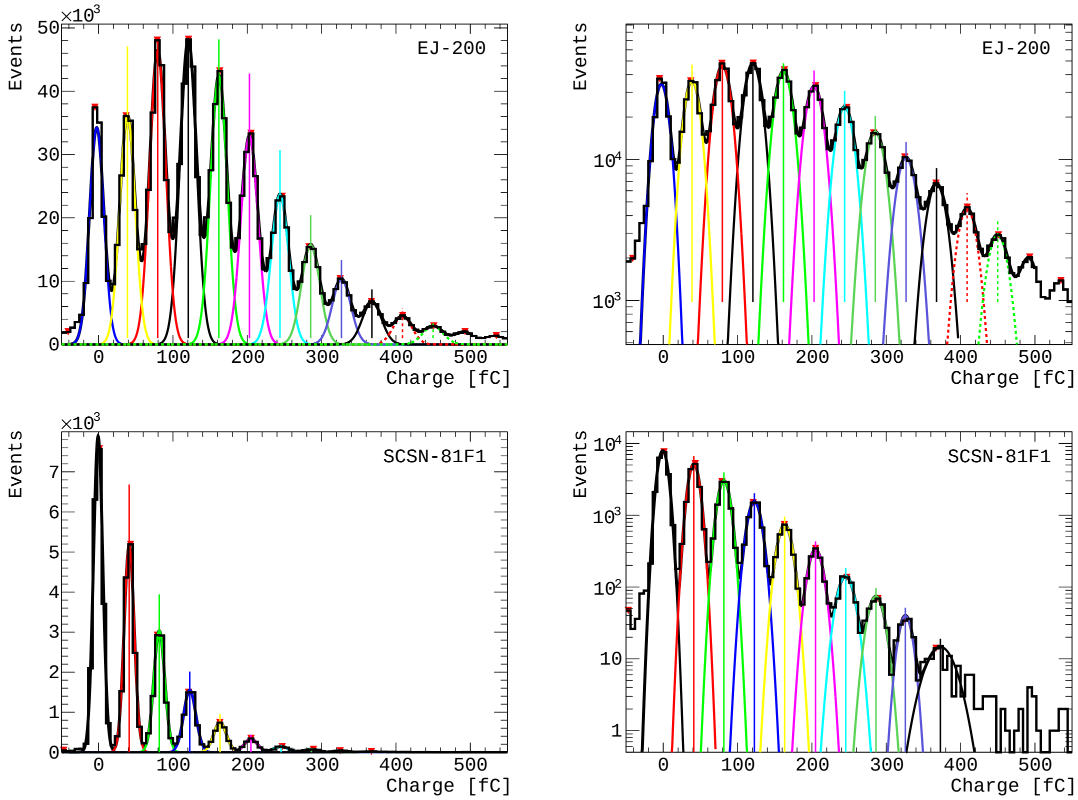

Figure 13. Example of multi-Gaussian fits to the charge spectra for the EJ-200 tile (upper), and the first SCSN-81 finger tile (lower), using linear (left) and logarithmic (right) scales. The colored Gaussians represent the fitted results; the vertical lines indicate the Gaussian functions included in the calculation of the estimator of the average number of photoelectrons.

this distance lies within the interval 41.5 ± 1.5 fC, which is very close to the value of 41 fC used to estimate the number of photoelectrons via the integration of contributions. The SiPM bias voltage was indeed set to obtain a distance between neighboring peaks of 41 fC. Thus, this result is in excellent agreement with the configuration of the photo sensors. A fit including a probability distribution that accounts for the effect of the after-pulsing has also been performed; the result suggests that after-pulsing is negligible. Two examples of the functional-form fits of the charge spectra are shown in figure 14. The fits have only six free parameters: pedestal peak location, separation between neighboring peaks, electronic noise standard deviation, contribution to the peak width dependent on the number of photoelectrons, average number of photoelectrons, cross-talk probability. They demonstrate that it is possible to obtain an adequate description of a SiPM spectrum over multiple orders of magnitude with a small number of free parameters.

Results. Table 2 summarizes the results of the two methods described in the previous paragraphs. The results of the functional-form fit, even after implementing the correction for cross-talk photoelectrons, are $\approx 20\%$ and 40% lower for σ and finger tiles than the estimators provided by the other methods. It is hard to obtain a high-quality fit due to the complexity of the fit function.

To further characterize the decrease in efficiency in the central region of the SCSN-81 σ tile, the fiducial region is divided into two parts: central (defined by the requirement that $-30 < x_{\text{hit}} < 0$ mm

2025 JINST 20 P01026

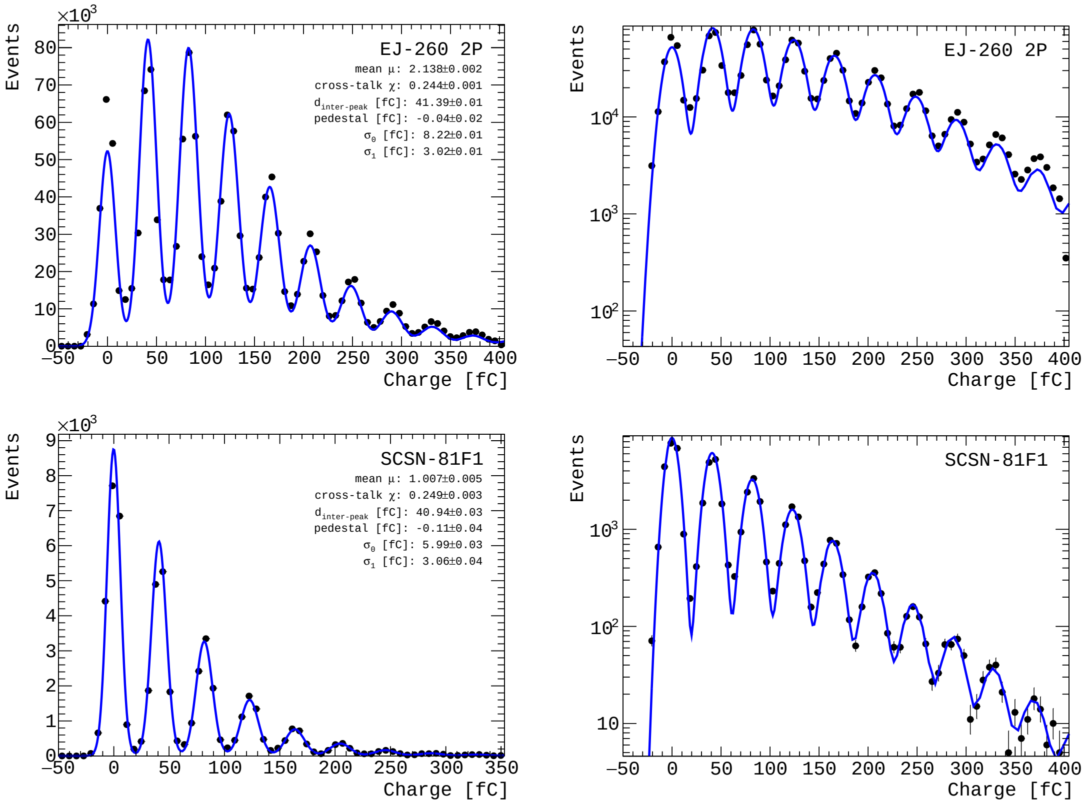

Figure 14. Example of functional-form fits to charge spectra for the EJ-260 2P tile (upper), and first SCSN-81 finger tile (lower), using linear (left) and logarithmic (right) scale. The fit parameters are reported in the linear-scale plot: μ is the average number of photons initiating the Geiger discharge in the SiPM; χ the probability of cross-talk; $d_{\text{inter-peak}}$ is the separation between neighboring peaks; pedestal indicates the location of the pedestal peak (it is consistent with zero, suggesting that the pedestal subtraction was correctly implemented); σ_0 and σ_1 are used to parameterize the width of the Gaussian peaks as follows: $\sigma_i^2 = \sigma_0^2 + i\sigma_1^2$.

and $-30 < y_{\text{hit}} < 0$ mm), and peripheral (complementary to the central region). The corresponding light yields are then measured separately in the two regions, using the two methods presented above. The efficiency profile suggests that the light yield should be smaller in the central region, which is farther from the wavelength-shifting readout fiber. This is indeed the case; though the observed drop of $\approx 3\%$ is expected to have a negligible impact on the energy resolution of the calorimeter.

4 Summary and conclusions

This study involves the measurement of the light yield and uniformity of irradiated plastic scintillators using a muon beam produced from the decay of a 150 GeV pion beam. The efficiency is measured relative to the x and y positions within the scintillator tile detectors to determine whether any color centers created during irradiation cause a change in the tile efficiency. The irradiated SCSN-81 σ tile is found to have a considerable reduction, about 50%, in the light yield relative to a similarly configured, unirradiated EJ-200 tile. This is expected, and consistent with studies presented in refs. [5, 19]. It is noted that the radiation damage affects the uniformity of the light yield by at most a few percent, with negligible impact on the resolution of the calorimeter. A more significant

2025 JINST 20 P01026

Table 2. Estimated number of photoelectrons emitted on average when a single minimum-ionizing particle (muon) crosses the scintillator tile. The parameter χ is the cross-talk probability, one of the parameters of the functional-form fit function. The quoted values are statistical uncertainties from the fit.

Tile	$\langle \text{PE} \rangle_{functional-form}$	χ	$\langle \text{PE} \rangle_{functional-form} / (1-\chi)$	$\langle \text{PE} \rangle_{integration\ of\ contributions}$
EJ-200	2.742 ± 0.002	0.235 ± 0.001	3.585 ± 0.004	4.365
EJ-260	2.316 ± 0.002	0.238 ± 0.001	3.040 ± 0.004	3.784
EJ-260 2P	2.138 ± 0.002	0.244 ± 0.001	2.826 ± 0.003	3.531
SCSN-81F1	1.007 ± 0.005	0.249 ± 0.003	1.340 ± 0.009	2.157
SCSN-81F2	1.191 ± 0.004	0.257 ± 0.002	1.602 ± 0.007	2.410
SCSN-81F3	1.085 ± 0.003	0.252 ± 0.002	1.451 ± 0.006	2.295
SCSN-81F4	1.042 ± 0.004	0.250 ± 0.002	1.390 ± 0.007	2.240
SCSN-81S	1.711 ± 0.002	0.268 ± 0.001	2.336 ± 0.003	3.026

dependence of the light yield on hit position is observed in the case of finger tiles, which at worst indicates an efficiency variation of about 40%.

Acknowledgments

The authors would like to thank CERN for the operations of the SPS accelerator; Dragoslav Lazic for supporting operations in the H2 test-beam area; Chuck Hurlbut (Eljen Technology) for the advice on scintillators, and the preparation of test samples; Janina Gielata (FNAL) for the preparation of optical connections. Individuals have received support from the Belgian Fonds de la Recherche Scientifique, and Fonds voor Wetenschappelijk Onderzoek; the Brazilian Funding Agencies (CNPq, CAPES, FAPERJ, FAPERGS, and FAPESP); SRNSF (Georgia); the Bundesministerium für Bildung und Forschung, the Deutsche Forschungsgemeinschaft (DFG), under Germany's Excellence Strategy — EXC 2121 "Quantum Universe" — 390833306, and under project number 400140256 - GRK2497, and Helmholtz-Gemeinschaft Deutscher Forschungszentren, Germany; the National Research, Development and Innovation Office (NKFIH) (Hungary) under project numbers K 128713, K 143460, and TKP2021-NKTA-64; the Department of Atomic Energy and the Department of Science and Technology, India; the Ministry of Science, ICT and Future Planning, and National Research Foundation (NRF), Republic of Korea; the Lithuanian Academy of Sciences; the Scientific and Technical Research Council of Turkey, and Turkish Energy, Nuclear and Mineral Research Agency; the National Academy of Sciences of Ukraine; the US Department of Energy.

References

[1] ATLAS collaboration, *The ATLAS Experiment at the CERN Large Hadron Collider*, 2008 *JINST* **3** S08003.

[2] CMS collaboration, *The CMS Experiment at the CERN LHC*, 2008 *JINST* **3** S08004.

[3] C. Zorn, *Fast scintillators for high radiation levels. 2: Plastic and liquid organic scintillators*, *Adv. Ser. Direct. High Energy Phys.* **9** (1992) 218.

2025 JINST 20 P01026

[4] Y.N. Kharzheev, *Radiation Hardness of Scintillation Detectors Based on Organic Plastic Scintillators and Optical Fibers*, Phys. Part. Nucl. **50** (2019) 42.

[5] CMS collaboration, *Measurements with silicon photomultipliers of dose-rate effects in the radiation damage of plastic scintillator tiles in the CMS hadron endcap calorimeter*, 2020 *JINST* **15** P06009 [arXiv:2001.06553].

[6] M. Aleksa et al., *Calorimeters for the FCC-hh*, arXiv:1912.09962.

[7] S. Liao et al., *A comparative study of the radiation hardness of plastic scintillators for the upgrade of the Tile Calorimeter of the ATLAS detector*, J. Phys. Conf. Ser. **645** (2015) 012021.

[8] CMS HCAL collaboration, *Brightness and uniformity measurements of plastic scintillator tiles at the CERN H2 test beam*, 2018 *JINST* **13** P01002 [arXiv:1709.08672].

[9] CMS collaboration, *CMS Technical Design Report for the Phase 1 Upgrade of the Hadron Calorimeter*, CERN-LHCC-2012-015 (2012) [DOI:10.2172/1151651].

[10] A. Heering et al., *Parameters of the preproduction series SiPMs for the CMS HCAL phase I upgrade*, Nucl. Instrum. Meth. A **824** (2016) 115.

[11] T. Zimmerman and J.R. Hoff, *The design of a charge integrating, modified floating point ADC chip*, IEEE J. Solid State Circuits **39** (2004) 895.

[12] A. Baumbaugh et al., *QIE10: a new front-end custom integrated circuit for high-rate experiments*, 2014 *JINST* **9** C01062.

[13] T. Roy et al., *QIE: Performance Studies of the Next Generation Charge Integrator*, 2015 *JINST* **10** C02009.

[14] D. Hare et al., *First large volume characterization of the QIE10/11 custom front-end integrated circuits*, 2016 *JINST* **11** C02052.

[15] F. Vasey et al., *The Versatile Link common project: feasibility report*, 2012 *JINST* **7** C01075.

[16] CMS CASTOR collaboration, *Design and test beam studies for the CASTOR calorimeter of the CMS experiment*, Nucl. Instrum. Meth. A **623** (2010) 225.

[17] V. Chmill et al., *On the characterisation of SiPMs from pulse-height spectra*, Nucl. Instrum. Meth. A **854** (2017) 70 [arXiv:1609.01181].

[18] W. Verkerke and D.P. Kirkby, *The RooFit toolkit for data modeling*, eConf C **0303241** (2003) MOLT007 [physics/0306116].

[19] CMS HCAL collaboration, *Dose rate effects in the radiation damage of the plastic scintillators of the CMS Hadron Endcap Calorimeter*, 2016 *JINST* **11** T10004 [*Erratum ibid.* **14** (2019) E08001] [arXiv:1608.07267].

2025 JINST 20 P01026

The CMS HCAL collaboration

Yerevan Physics Institute, Yerevan, Armenia

A. Gevorgyan, A. Petrosyan, A. Tumasyan

Universiteit Antwerpen,• Antwerpen, Belgium

M. Van De Klundert, H. Van Haevermaet, P. Van Mechelen, A. Van Spilbeeck

Centro Brasileiro de Pesquisas Fisicas,• Rio de Janeiro, Brazil

G.A. Alves, C. Hensel

Universidade do Estado do Rio de Janeiro,• Rio de Janeiro, Brazil

W.L. Aldá Júnior, W. Carvalho, J. Chinellato[1], C. De Olivera Martins, D. Matos Figueiredo, C. Mora Herrera, H. Nogima, W.L. Prado Da Silva, E.J. Tonelli Manganote, A. Vilela Pereira

Charles University, Prague, Czech Republic

M. Finger Jr.[2], M. Finger[2]

Georgian Technical University, Tbilisi, Georgia

G. Adamov, I. Lomidze, T. Toriashvili[3], Z. Tsamalaidze[3]

Deutsches Elektronen-Synchrotron, Hamburg, Germany

K. Borras[4], A. Campbell, F. Engelke[4], D. Krücker, I. Martens, L. Wiens[4]

MTA-ELTE Lendület CMS Particle and Nuclear Physics Group, Eötvös Loránd University, Budapest, Hungary

M. Csanád, S. Lökös[5], A. Feherkuti, G. Pásztor, O. Surányi, G.I. Veres

Indian Institute of Science Education and Research (IISER),• Pune, India

V. Hegde, K. Kothekaar, S. Pandey, S. Sharma

Panjab University,• Chandigarh, India

S.B. Beri, B. Bhawandeep, R. Chawla, A. Kalsi, A. Kaur, M. Kaur, G. Walia

Saha Institute of Nuclear Physics,• Kolkata, India

S. Bhattacharya, S. Ghosh, S. Nandan, A. Purohit, M. Sharan

Tata Institute of Fundamental Research-B,• Mumbai, India

S. Banerjee, S. Bhattacharya, S. Chatterjee, P. Das, M. Guchait, S. Jain, S. Kumar, M. Maity, G. Majumder, K. Mazumdar, M. Patil, T. Sarkar

Kyungpook National University, Daegu, Korea

S. Sekmen

Vilnius University, Vilnius, Lithuania

A. Juodagalvis

2025 JINST 20 P01026

Çukurova University, Physics Department, Science and Art Faculty, Adana, Turkey
D. Agyel, F. Boran, S. Damarseckin, Z.S. Demiroglu, F. Dolek, I. Dumanoglu[6], E. Eskut, G. Gokbulut, Y. Guler[7], E. Gurpinar Guler[7], C. Isik, E.E. Kangal, O. Kara, A. Kayis Topaksu, U. Kiminsu, G. Onengut, K. Ozdemir[8], E. Pinar, A. Polatoz, A.E. Simsek, B. Tali[9], U.G. Tok, S. Turkcapar, E. Uslan, I.S. Zorbakir

Middle East Technical University, Physics Department,[•] Ankara, Turkey
B. Bilin[10], G. Karapinar, A. Murat Guler, K. Ocalan[11], M. Yalvac[12], M. Zeyrek

Bogazici University, Istanbul, Turkey
B. Akgun, I.O. Atakisi, E. Gülmez, M. Kaya[13], O. Kaya[14], S. Tekten[15], E.A. Yetkin[54], T. Yetkin[16]

Istanbul Technical University, Istanbul, Turkey
K. Cankocak[6], S. Sen[17]

Istanbul University, Istanbul, Turkey
O. Aydilek, S. Cerci[9], B. Hacisahinoglu, I. Hos[18], B. Isildak[16], B. Kaynak, S. Ozkorucuklu, O. Potok, H. Sert, C. Simsek, D. Sunar Cerci[9], C. Zorbilmez

Institute for Scintillation Materials of National Academy of Science of Ukraine, Kharkiv, Ukraine
A. Boyarintsev, B. Grynyov

National Science Centre, Kharkiv Institute of Physics and Technology, Kharkiv, Ukraine
L. Levchuk, V. Popov, P. Sorokin

University of Bristol, Bristol, United Kingdom
H. Flacher

Baylor University, Waco, Texas, U.S.A.
S. Abdullin, B. Caraway, J. Dittmann, K. Hatakeyama, A.R. Kanuganti, B. McMaster, M. Saunders, J. Wilson

The University of Alabama, Tuscaloosa, Alabama, U.S.A.
P. Bunin[2], A. Buccilli[19], S.I. Cooper, C. Henderson[20], C.U. Perez, P. Rumerio[21], C. West

Boston University, Boston, Massachusetts, U.S.A.
D. Arcaro, C. Cosby, Z. Demiragli, D. Gastler, E. Hazen, J. Rohlf

Brown University, Providence, Rhode Island, U.S.A.
M. Hadley, U. Heintz, T. Kwon, G. Landsberg, K.T. Lau, Z. Mao, X. Yan, D.R. Yu[22]

University of California, Riverside, Riverside, California, U.S.A.
J.W. Gary, G. Karapostoli[23], O.R. Long

2025 JINST 20 P01026

University of California, Santa Barbara - Department of Physics, Santa Barbara, California, U.S.A.

R. Bhandari, R. Heller, D. Stuart, J.H. Yoo

California Institute of Technology, Pasadena, California, U.S.A.

Y. Chen, J. Duarte, J.M. Lawhorn, M. Spiropulu

Fairfield University, Fairfield, Connecticut, U.S.A.

D. Winn

Fermi National Accelerator Laboratory, Batavia, Illinois, U.S.A.

A. Apresyan, A. Apyan[24], S. Banerjee[25], F. Chlebana, Y. Feng, J. Freeman, D. Green, J. Hirschauer, U. Joshi, K.H.M. Kwok, D. Lincoln, S. Los, C. Madrid, N. Pastika, K. Pedro, W.J. Spalding, S. Tkaczyk

Florida International University,• Miami, Florida, U.S.A.

S. Linn, P. Markowitz

Florida State University, Tallahassee, Florida, U.S.A.

V. Hagopian, T. Kolberg, G. Martinez, O. Viazlo

Florida Institute of Technology, Melbourne, Florida, U.S.A.

M. Hohlmann, R. Kumar Verma, D. Noonan, F. Yumiceva[26]

The University of Iowa, Iowa City, Iowa, U.S.A.

M. Alhusseini, B. Bilki[27], D. Blend, K. Dilsiz[28], L. Emediato, R.P. Gandrajula, M. Herrmann, O.K. Köseyan, J.-P. Merlo, A. Mestvirishvili[29], M. Miller, H. Ogul[30], Y. Onel, A. Penzo, D. Southwick, E. Tiras[31], J. Wetzel

The University of Kansas, Lawrence, Kansas, U.S.A.

A. Al-bataineh[32], J. Bowen[33], C. Le Mahieu, W. McBrayer, J. Marquez, M. Murray, M. Nickel, S. Popescu, C. Smith, Q. Wang

Kansas State University, Manhattan, Kansas, U.S.A.

K. Kaadze, D. Kim, Y. Maravin, A. Mohammadi[25], J. Natoli, D. Roy, L.K. Saini[34]

University of Maryland, College Park, Maryland, U.S.A.

E. Adams, A. Baden, O. Baron, A. Belloni[*], J.D. Calderon[35], Y.M. Chen, C. Coldsmith[36], S.C. Eno, C. Ferraioli[37], T. Grassi, N.J. Hadley, A. Hunt[38], G.Y. Jeng[39], R.G. Kellogg, T. Koeth, J. Kunkle[40], Y. Lai, S. Lascio, A.C. Mignerey, S. Nabili, C. Palmer, C. Papageorgakis, F. Ricci-Tam[41], M. Seidel[42], Y.H. Shin[43], L. Wang, K. Wong, Z. Yang, Y. Yao[44]

Massachusetts Institute of Technology, Cambridge, Massachusetts, U.S.A.

M. D'Alfonso, M. Hu, M. Klute[45]

University of Minnesota, Minneapolis, Minnesota, U.S.A.

B. Crossman, J. Hiltbrand, M. Krohn, J. Mans, M. Revering, N. Strobbe

2025 JINST 20 P01026

University of Notre Dame, Notre Dame, Indiana, U.S.A.

A. Heering, Y. Musienko[2], R. Ruchti, M. Wayne

Princeton University, Princeton, New Jersey, U.S.A.

A.D. Benaglia, W. Chung, G. Kopp, T. Medvedeva, K. Mei, C. Tully

University of Rochester, Rochester, New York, U.S.A.

A. Bodek, P. de Barbaro, C. Fallon, T. Ferbel[†], M. Galanti, A. Garcia-Bellido, A. Khukhunaishvili, R. Taus, D. Vishnevskiy, M. Zielinski

Rutgers, The State University of New Jersey, Piscataway, New Jersey, U.S.A.

B. Chiarito, J.P. Chou, S.A. Thayil, H. Wang

Texas Tech University, Lubbock, Texas, U.S.A.

N. Akchurin, J. Damgov, F. De Guio[46], S. Kunori, K. Lamichhane, S.W. Lee, T. Mengke, S. Muthumuni, S. Undleeb, I. Volobouev, Z. Wang, A. Whitbeck

University of Virginia, Charlottesville, Virginia, U.S.A.

G. Cummings, S. Goadhouse, J. Hakala, R. Hirosky

Authors affiliated with
an institute or an international laboratory covered by a cooperation agreement with CERN

V. Alexakhin, V. Andreev, Yu. Andreev, M. Azarkin, A. Belyaev, S. Bitioukov[†], E. Boos, O. Bychkova, M. Chadeeva, V. Chekhovsky, R. Chistov[47], M. Danilov, A. Demianov, A. Dermenev, M. Dubinin[48], L. Dudko, D. Elumakhov, V. Epshteyn[49], Y. Ershov, A. Ershov, V. Gavrilov, I. Golutvin[†], A. Gribushin, A. Kalinin[50], A. Kaminskiy, A. Karneyeu, L. Khein, M. Kirakosyan, V. Klyukhin, O. Kodolova[51], V. Krychkine, A. Kurenkov, A. Litomin, N. Lychkovskaya, V. Makarenko, P. Mandrik, P. Moisenz[†], S. Obraztsov, A. Oskin, P. Parygin[52], V. Petrov, S. Petrushanko, S. Polikarpov[47], E. Popova[50], V. Rusinov, R. Ryutin, V. Savrin, D. Selivanova, V. Smirnov, A. Snigirev, A. Sobol, A. Stepennov[53], E. Tarkovskii, A. Terkulov, D. Tlisov[†], I. Tlisova, R. Tolochek, M. Toms[45], A. Toropin, S. Troshin, A. Volkov, A. Zarubin, B. Yuldashev, A. Zhokin

[*] *Corresponding author*
[†] *Deceased*
[•] *No longer in CMS HCAL Collaboration*
[1] *Also at Universidade Estadual de Campinas, Campinas, Brazil*
[2] *Also at an institute or an international laboratory covered by a cooperation agreement with CERN*
[3] *Also at Tbilisi State University, Tbilisi, Georgia*
[4] *Also at RWTH Aachen University, III. Physikalisches Institut A, Aachen, Germany*
[5] *Also at Karoly Robert Campus, MATE Institute of Technology, Gyongyos, Hungary*
[6] *Also at Near East University, Research Center of Experimental Health Science, Nicosia, Turkey*
[7] *Also at Konya Technical University, Konya, Turkey*
[8] *Also at Piri Reis University, Istanbul, Turkey*
[9] *Also at Adiyaman University, Adiyaman, Turkey*
[10] *Also at CERN, Geneva, Switzerland*
[11] *Also at Necmettin Erbakan University, Konya, Turkey*
[12] *Also at Bozok Universitetesi Rektörlügü, Yozgat, Turkey*
[13] *Also at Marmara University, Istanbul, Turkey*

[14] *Also at Milli Savunma University, Istanbul, Turkey*
[15] *Also at Kafkas University, Kars, Turkey*
[16] *Now at Yildiz Technical University, Istanbul, Turkey*
[17] *Also at Hacettepe University, Ankara, Turkey*
[18] *Also at Istanbul University — Cerrahpasa, Faculty of Engineering, Istanbul, Turkey*
[19] *Now at Bond, San Francisco, U.S.A.*
[20] *Now at University of Cincinnati, Cincinnati, U.S.A.*
[21] *Also at Università di Torino, Torino, Italy*
[22] *Now at University of Nebraska, Lincoln, U.S.A.*
[23] *Now at National Technical University of Athens, Athens, Greece*
[24] *Now at Brandeis University, Waltham, U.S.A.*
[25] *Now at University of Wisconsin-Madison, Madison, U.S.A.*
[26] *Now at Northrop Grumman, Linthicum Heights, U.S.A.*
[27] *Also at Beykent University, Istanbul, Turkey*
[28] *Also at Bingol University, Bingol, Turkey*
[29] *Also at Georgian Technical University, Tbilisi, Georgia*
[30] *Also at Sinop University, Sinop, Turkey*
[31] *Also at Erciyes University, Kayseri, Turkey*
[32] *Now at Yarmouk University, Irbid, Jordan*
[33] *Now at Baker University, Baldwin City, U.S.A.*
[34] *Now at Gallagher Basset, Schaumburg, U.S.A.*
[35] *Now at NOAA, National Oceanic and Atmospheric Administration, U.S.A.*
[36] *Now at Northon Grumman Sperry Marine, Huntington Station, U.S.A.*
[37] *Now at Windfall Data, Novato, U.S.A.*
[38] *Now at Accenture Federal Services, Greenbelt, U.S.A.*
[39] *Now at ArcPoint Forensics, Sarasota, U.S.A.*
[40] *Now at Comprehensive Nuclear-Test-Ban Treaty Organization — CTBTO, Vienna, Austria*
[41] *Now at Sigmoid Health, Santa Clara, U.S.A.*
[42] *Now at Riga Technical University, Riga, Latvia*
[43] *Now at Mars Auto, Inc., Seoul, South Korea*
[44] *Now at University of California, Davis, Davis, U.S.A.*
[45] *Now at Karlsruhe Institute of Technology, Karlsruhe, Germany*
[46] *Now at Università degli Studi di Milano Bicocca, Milano, Italy*
[47] *Also at another institute or international laboratory covered by a cooperation agreement with CERN*
[48] *Also at California Institute of Technology, Pasadena, California, U.S.A.*
[49] *Now at Istanbul University, Istanbul, Turkey*
[50] *Now at University of Maryland, College Park, U.S.A.*
[51] *Also at Yerevan Physics Institute, Yerevan, Armenia*
[52] *Now at University of Rochester, Rochester, New York, U.S.A.*
[53] *Now at University of Cyprus, Nicosia, Cyprus*
[54] *Also at İstanbul Bilgi University, İstanbul, Turkey*

2025 JINST 20 P01026